Optical design and diffraction analysis for AIRES: an Airborne InfraRed Echelle Spectometer

Michael R. Haas*
NASA-Ames Research Center, MS 245-6, Moffett Field, CA 94035-1000

ABSTRACT

The optical design is presented for a long-slit grating spectrometer known as AIRES (Airborne InfraRed Echelle Spectrometer). The instrument employs two gratings in series: a small order sorter and a large steeply blazed echelle. The optical path includes four pupil and four field stops, including two narrow slits. A detailed diffraction analysis is performed using GLAD by Applied Optics Research to evaluate critical trade-offs between optical throughput, spectral resolution, and system weight and volume. The effects of slit width, slit length, oversizing the second slit relative to the first, on- vs off-axis throughput, and clipping at the pupil stops and other optical elements are discussed.

Keywords: Diffraction, grating, infrared, SOFIA, spectrometer

1. INTRODUCTION

The Airborne InfraRed Echelle Spectrometer (AIRES) is a potential second-generation facility instrument for the Stratospheric Observatory for Infrared Astronomy (SOFIA). The instrument is designed primarily for studies of the interstellar medium and would use an existing 76° blaze angle (R4) echelle to combine high-resolution spectroscopy ($\lambda/\Delta\lambda \approx 70000 - 5000$) with diffraction-limited imaging in the cross-dispersion direction. The spectroscopic focal plane is sized to accommodate three two-dimensional detector arrays to provide good sensitivity over 3.6 octaves in wavelength (17 – 210 μm). A fourth infrared array images the entrance slit of the spectrometer against the surrounding sky to determine source morphology and verify telescope pointing. The scientific motivation and advantages of cryogenically cooled, long-slit grating spectrometers such as AIRES are well known.[1,2]

The resolution of a grating spectrometer is ~$2L/\lambda$, where L is the projected length of the grating along the incoming collimated beam. To achieve high resolution in the far-infrared, a large grating is essential. The AIRES grating is 267 × 1067 mm; it has been successfully ruled and is diffraction limited near 4 μm.[3] The available instrument volume on SOFIA is roughly cylindrical with a diameter of ~1 m and a length of ~2 m. It has been extremely challenging to cryogenically package this large echelle, its 5-m collimator, an order-sorting 'predisperser' grating, the detector arrays, and other optics in such a compact volume, while maintaining mechanical stability, enabling optical alignment, and providing access for servicing.

The optical design has been completed using the basic concepts outlined in the preliminary design,[1] but with several significant improvements, as described below. A detailed treatment of diffraction effects within the instrument has been carried out to aid in sizing the optics, including the long slits, and estimating system throughput and performance.

2. OPTICAL DESIGN AND LAYOUT

AIRES was designed using Code V, a geometrical ray-tracing program. The principal optical components in the spectrometer are (a) the front-end optics, which include a cold Lyot stop, a field rotator, plate-scale changing optics, and two filter wheels; (b) the predisperser, which contains selectable entrance and exit slits and five small carousel-mounted gratings operating in first order to sort orders for the echelle; (c) the echelle grating and its collimator, which provide the

* Correspondence: Email: mhaas@mail.arc.nasa.gov; Telephone: 650 604 5511; FAX: 650 604 3625.

high dispersion; and (d) four detector arrays and two short-wavelength plate-scale changing cameras. Figure 1 shows a side view of the optics mounted on a cryogenic baseplate/optical bench. In this figure, the system is split into three parts for clarity; the upper two views join at PS and the two left-most views join at ES. The elements F3, PS, & P1 and E1, ES, & E2 are physically separated in the dimension normal to the page.

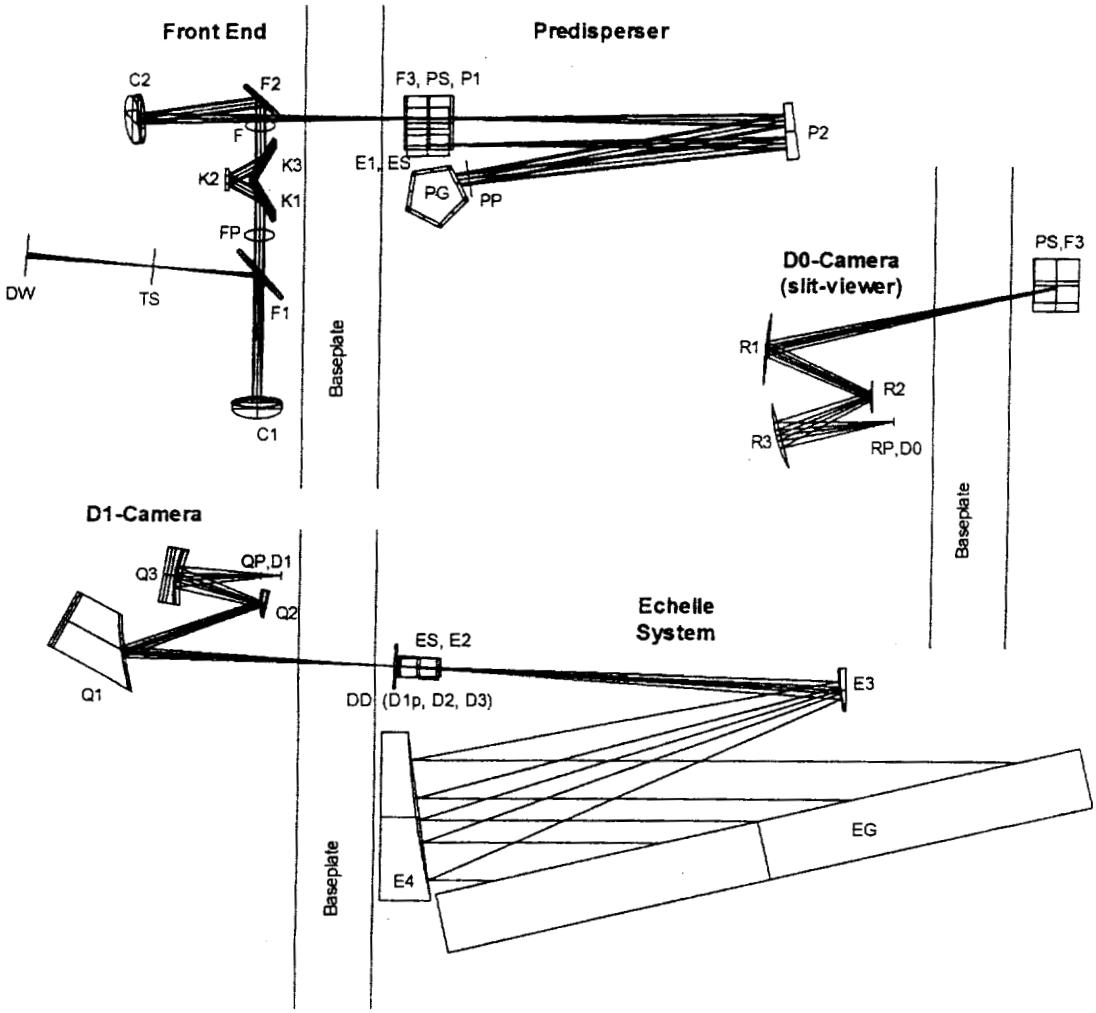

Figure 1. A side view of the AIRES optical system is shown with the central field traced. The three portions of the instrument can be properly registered by overlaying the three instances of the baseplate.

Figure 2 is a layout of the spectrometer with lenses replacing mirrors and grisms replacing gratings; the dispersion direction is normal to the page. In actuality, the only transmissive elements are the dewar window (DW) and the filters (FP, F). In this unfolded layout, the field stops are readily distinguishable from the pupil stops, as the former contain five ray bundles corresponding to the five input fields and the latter contain three ray bundles indicating the center and edges of the telescope secondary image. Double passed elements are physically separated in this layout, so the second instance of a surface is identified by the suffix '_2'.

Light enters through the dewar window (DW) on the left in Figures 1 and 2 and is focused by the telescope at field stop TS. The off-axis paraboloid C1 collimates the beam and forms a pupil (image of the telescope secondary) at the cold Lyot stop (K2), which operates in reflection. Field rotation is accomplished by a compact, rotating K-mirror assembly consisting of three flats (K1 – K3). The second off-axis paraboloid C2 refocuses the beam at the predisperser entrance

slit (PS) and reduces the plate scale by 20%. The folding flats F1, F2, and F3 facilitate packaging. The filter (F) and Fabry-Perot (FP) wheels are located on either side of the K-mirror to minimize the diameter of these elements (~50 mm). The Fabry-Perot wheel can hold both fixed etalons for wavelength verification and additional blocking filters, as desired. A major change from the preliminary design[1] is the compact, nonpowered K-mirror mounted directly on the baseplate, which simplifies alignment, increases stability, and conserves space.

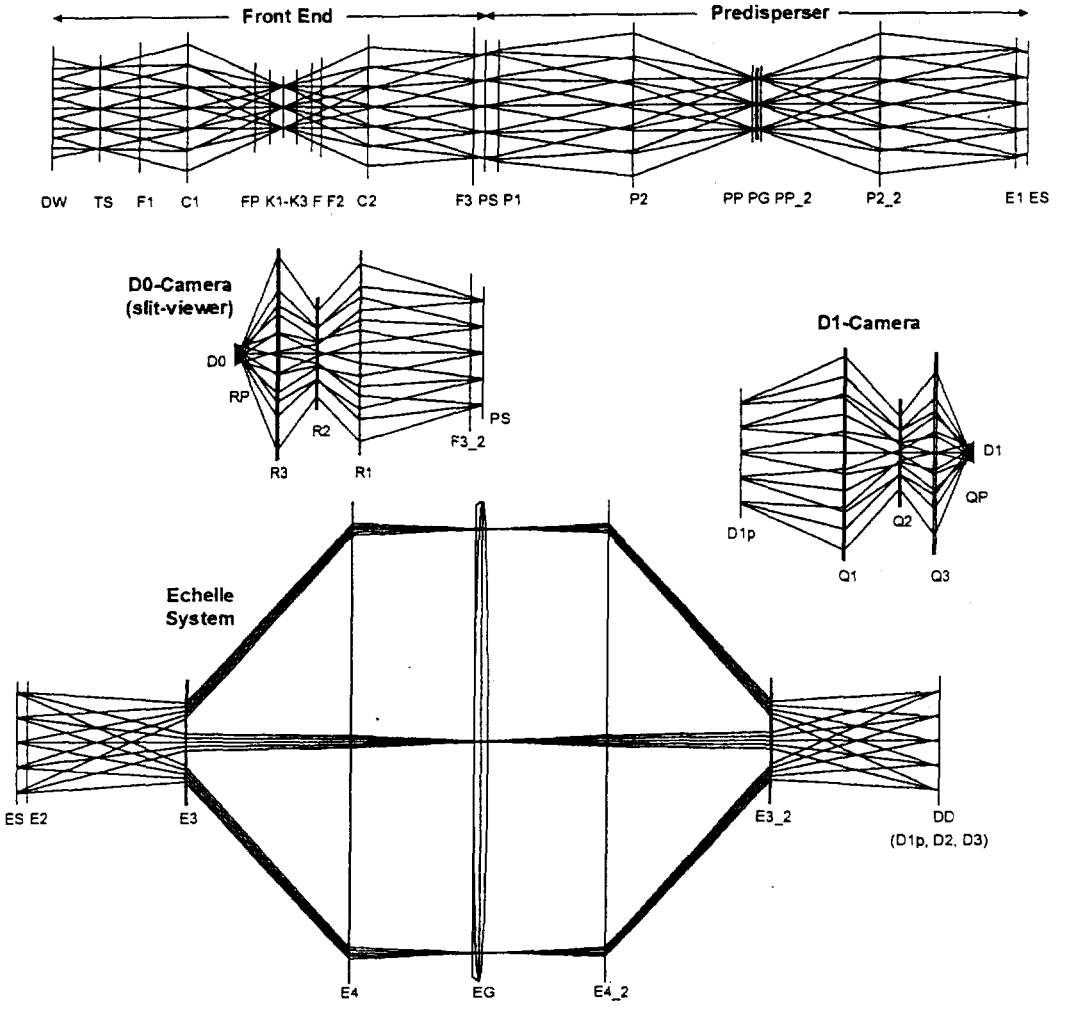

Figure 2. A lens-equivalent model of the AIRES optical system is traced for five field points. The system is broken into four parts for clarity; overlay the surfaces with common labels to connect the parts. The vertical scale is expanded by a factor of eight relative to the horizontal scale to facilitate viewing.

At PS, light takes one of two paths since the surface surrounding this entrance slit is reflective and tilted ~6° relative to the input beam. The reflected light passes back through the baseplate to the slit-viewing camera (*i.e.*, mirrors R1, R2, and R3) via a second hit on flat F3 (*i.e.*, F3_2). A pupil is formed at RP and PS is reimaged at D0, where a two-dimensional infrared array detector is located.

The light transmitted by the entrance slit (PS) enters the predisperser, which contains elements PS to ES. The off-axis ellipsoid P1 is located near the PS slit and, in conjunction with the paraboloidal collimating mirror P2, reimages the K2 pupil at the predisperser grating PG. The diffracted beam from grating PG returns to mirror P2, which forms a focus at the exit slit ES with the help of mirror E1. The ellipsoid E1 also reimages the pupil at PG on the center of the echelle

grating EG with the help of the echelle collimator (E3/E4). The pupils are located at PG and EG to reduce beam walk, facilitate baffling, and minimize the size of these optical elements (this is particularly important for EG). The PS and ES slits are mounted on rotating wheels and the five predisperser gratings are mounted on a carousel. An important change from the preliminary design[1] is that the predisperser now operates in non-Littrow mode ($\alpha \neq \beta$, $\gamma = 0$, see Appendix A). This eliminates field rotation in the predisperser and avoids ~~the need for~~ rotation mechanisms on the individual ES slits.

The echelle collimator is an off-axis Cassegrain design (*i.e.*, hyperboloid E3 and paraboloid E4), which should be much easier to manufacture, measure, and align then the anamorphic design considered earlier.[1] Injection into the collimator occurs via flat E2 and the diffracted beam from EG is refocused in the primary spectroscopic focal plane (DD) by a return pass through the collimator. Mirror E2 and the spectroscopic arrays are side-by-side, but out of plane, in a quasi-Littrow configuration ($\alpha = \beta$, $\gamma \neq 0$). The dispersion directions for PG and EG are coplanar to maintain good image quality and high grating throughput. The DD focal plane contains the mid-wavelength array (D2), the long-wavelength array (D3), and an intermediate focus (D1p) for the short-wavelength array (D1). The three-mirror anastigmat camera (*i.e.*, mirrors Q1, Q2, and Q3) forms a pupil at QP and a focus at D1. Both the D0- and D1-cameras change the plate scale by a factor of five to accommodate the typical format of commercial arrays.

For the final AIRES design, the focal length of the predisperser collimator is $F_p = 635$ mm, the focal length of the echelle collimator is $F_e = 5205$ mm, the operational range for each predisperser grating is $14° < \eta_p < 24°$, and the operational range for the echelle grating is $62° < \beta_e < 79°$. The five predisperser gratings are 41 × 64 mm with a blaze angle of 19° and ruling spacings of 35, 58, 95, 157, and 260 μm. The echelle grating is 267 × 1067 mm with a blaze angle of 76° and a ruling spacing of 976 μm. The plate scales at TS, PS, ES, and DD are 4.25, 3.36, 3.47, and 3.50 arcsec/mm, respectively. The D2 and D3 arrays are 32.5 × 48.8 mm (dispersion × spatial), D1p is 48.8 × 48.8 mm, and D1 is 9.6 × 9.6 mm, all before oversizing (see below).

3. BASELINE APERTURE AND SLIT SIZES

Clear Aperture Sizes: Modern designs for infrared imagers typically oversize the radii of clear apertures by five or more Airy rings beyond the geometric field of view for the furthest off-axis detector pixel.[4,5] This produces uniform illumination over the exit pupil, which minimizes vignetting, simplifies flat fielding, and facilitates 'sky noise' compensation.[5] For the *f*/number of the SOFIA telescope, five Airy rings correspond to a distance ~0.1 $\lambda_{\mu m}$ mm, where $\lambda_{\mu m}$ is the wavelength in microns (*e.g.*, 20 mm on the radius of a clear aperture at 200 μm).

This simple, additive sizing rule is inappropriate for spectrometers with diffraction-limited entrance slits, multiple pupil and field stops, and the large diameter collimators required to achieve high dispersion. For example, the AIRES' design has field stops at TS, PS, ES, and DD and pupil stops at K2, PG, EG, and QP (see Figure 2). These stops differ radically in size and seem more suited to a multiplicative, rather than an additive margin for diffraction. It is particularly important to avoid oversizing optics when instrument volume is highly constrained, since this may preclude a number of otherwise attractive and efficient design options. Hence, the mirrors were modestly oversized using the following procedure: (a) the telescope tertiary was oversized by 10%; (b) each array in the spectroscopic focal plane (DD) was oversized by 4 mm on all sides (*i.e.*, by 17%); (c) the resulting extreme spatial/spectral rays were used to define a minimum clear aperture at each surface; and (d) these minimum clear apertures were increased by 5 mm on all sides to provide 'baseline' apertures for the mirrors, gratings, baffles, and filters, and for the field stops at TS and DD. The other field stops (*i.e.*, the long slits PS and ES) were sized as described below; the pupil stops were retained at the 10% oversizing described above. At 210 μm, this procedure gave margins of 5 Airy rings at the largest apertures (*e.g.*, E4), but more typical margins of a few Airy rings.

PS Slit Width: For a long-slit spectrometer, selecting the proper slit width is a trade-off between resolution and throughput. For AIRES, this issue is complex because there are two slits in series – the first slit (PS) defines the field of view on the sky and determines the resolution; the second slit (ES) blocks unwanted echelle orders in the predisperser.

If the front-end optics are of sufficient size and quality, then the point spread function (PSF) at the entrance slit is dominated by telescope diffraction at long wavelengths. For a centrally obstructed telescope, the PSF is:

$$I(x)/I(0) = (2/(1-\varepsilon^2))^2 (J_1(x)/x - \varepsilon J_1(\varepsilon x)/x)^2, \quad (1)$$

where $J_1(x)$ is the first order Bessel Function, ε is the linear obscuration of the primary, $x = kD\omega/2$, $k = 2\pi/\lambda$, D = effective diameter of the primary, and ω = field angle on the sky.[6] For SOFIA, $\varepsilon = 0.26$ and the PSF has its first dark ring at ~1.1 λ/D or ~0.09 $\lambda_{\mu m}$ arcsec. Integrating Equation (1) over a long slit, half the light is transmitted for a width of ~0.72 λ/D or ~0.058 $\lambda_{\mu m}$ arcsec.

Doubling this slit width increases the transmission to 74%; further increases in width provide only modest increases in transmission (*cf* Figure 7). Hence, the AIRES' predisperser slits (PS) are sized logarithmically from ~λ/D at 17 μm to ~2λ/D at 210 μm and have widths of 1.3, 2.0, 2.9, 4.4, 6.6, 10.0, 15.1, 22.7, and 34.3 arcsec. Using the plate scale at PS, these correspond to physical widths of 0.4 to 10.2 mm.

ES Slit Width: The predisperser exit (or echelle entrance) slit ES must be wide enough to provide good throughput, but narrow enough to block unwanted echelle orders. To avoid geometric light loss, each point on the PS slit must map onto a point on the ES slit. The variation in the off-axis angle γ along the length of the PS slit produces parabolic field curvature[7] (or smile) at ES. The required oversizing can be minimized if the ES slit is shaped to match the field curvature at $\eta_p = 19°$, the mean predisperser grating angle. For the operational range of angles, the differential field curvature can be accommodated by oversizing ES relative to PS by an amount:

$$\Delta y_{field\ curvature} = 0.03\ |\eta_p - 19°|\ \text{mm}. \quad (2)$$

In addition, each point across the image of the PS slit formed at ES must pass the full range of wavelengths dispersed across the operational detector array by the echelle. This range of wavelengths (*i.e.*, the total bandpass) is:

$$\Delta\lambda_{array\ bandpass} = \lambda\ \Delta y_{dd}\ /(2F_e \tan \beta_e), \quad (3)$$

where Δy_{dd} is the linear size of the array in the dispersion direction (see Appendix A). Dispersion in the predisperser physically separates this range of wavelengths at ES by:

$$\Delta y_{dispersion} = 2F_p \tan \eta_p\ \Delta\lambda_{array\ bandpass}/\lambda = (F_p/F_e)\ (\tan \eta_p/\tan \beta_e)\ \Delta y_{dd}. \quad (4)$$

Hence, to geometrically pass all rays from PS for all relevant wavelengths, the ES slit must have a geometric width

$$\Delta y_{ES} \geq \Delta y_{PS} + \Delta y_{field\ curvature} + \Delta y_{dispersion}, \quad (5)$$

where Δy_{PS} is the width of the PS image formed at ES.

At the same time, the ES slit must remain small compared to the separation of echelle orders for effective order sorting. From the grating equation (Appendix A), the adjacent echelle orders are separated from the desired order m by:

$$\Delta\lambda_- = \lambda_{m-1} - \lambda_m = 2d_e \sin \beta_e\ [1/(m-1) - 1/m] = \lambda/(m-1), \text{ and} \quad (6)$$

$$\Delta\lambda_+ = \lambda_m - \lambda_{m+1} = 2d_e \sin \beta_e\ [1/m - 1/(m+1)] = \lambda/(m+1), \quad (7)$$

or simply, $\lambda/\Delta\lambda \approx m$ for large m. Hence, at ES the predisperser physically separates wavelengths corresponding to adjacent echelle orders by a distance:

$$\Delta y_{order} = 2F_p \tan \eta_p\ \Delta\lambda/\lambda = 2F_p \tan \eta_p/m. \quad (8)$$

Figure 3 graphically compares Δy_{ES} and Δy_{order} for $17 < \lambda < 210$ μm assuming the standard AIRES parameters and employing the largest echelle order at each wavelength which has $\beta_e < 77°$. The large, bold curves across the top of the figure show Δy_{order}, the distance to the next order in the plane of the ES slit. The large discontinuities correspond to

changes in predisperser grating; the small jumps show the echelle order changing from m = 112 on the far left to m = 9 on the far right. In some cases, echelle orders are split by changes in predisperser grating.

The medium-weight curves across the bottom of Figure 3 show Δy_{ES}, the minimum geometric width of the ES slit at each wavelength. Each horizontal 'cluster' of line segments corresponds to a particular predisperser grating/PS slit combination. The three to four clusters stacked vertically at each wavelength correspond to the different PS slit widths considered. The lowest horizontal cluster at each wavelength corresponds to the narrowest PS slit that passes more than 50% of the radiation or the smallest available slit, whichever is larger. The uppermost horizontal cluster at each wavelength corresponds to the largest PS slit with a width ≤5 times the minimum slit width. The small jumps within each horizontal cluster represent changes in echelle order; the discontinuities at 42 and 125 μm correspond to changes in detector pitch.

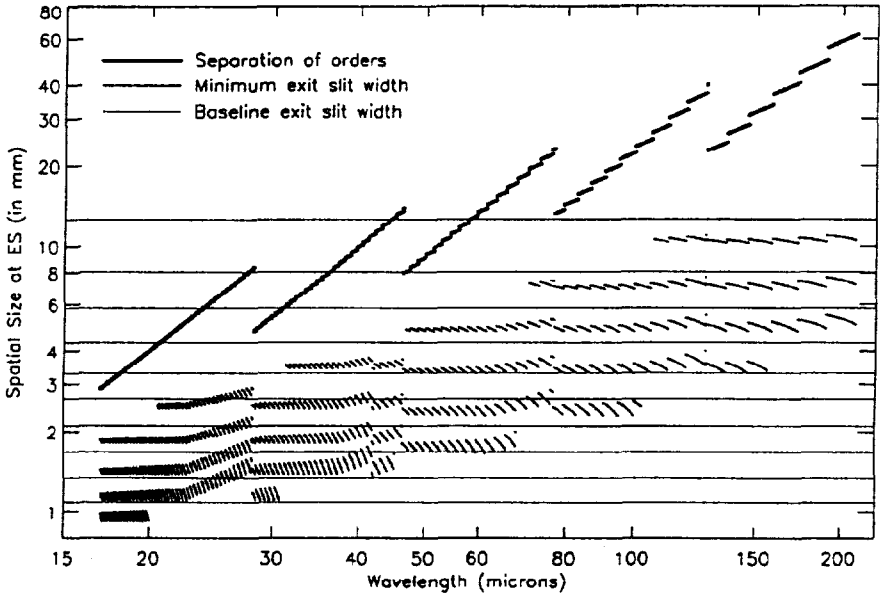

Figure 3. A graphical comparison of Δy_{order}, the separation of orders, Δy_{ES}, the minimum exit slit width, and the ten baseline exit slit widths is shown as a function of wavelength.

For each wavelength and PS slit width, any ES slit width between Δy_{ES} and Δy_{order} is acceptable from a geometrical point of view, since it passes all the light from PS while blocking adjacent orders. Based on several plots of this type for different echelle angles within the allowed range, the ES slit widths were baselined at 1.1, 1.3, 1.7, 2.1, 2.6, 3.3, 4.3, 5.8, 8.1, and 12.7 mm and are indicated by the light-weight horizontal lines in Figure 3. As an example, Figure 3 shows four PS slits at 19 μm. For the smallest (*i.e.*, 0.4 mm), there are 6 ES slit widths that appear acceptable (i.e, they pass all geometric light and block adjacent orders). The next section evaluates the effects of diffraction on this model.

4. DIFFRACTION ANALYSIS

Fresnel (near-field) and Fraunhofer (far-field) diffraction can be evaluated analytically for a number of specialized geometries,[6,8] but for the complex geometry typically found in a real instrument, a numerical ray trace program is the only practical solution. The present analysis was performed with a physical optics program called General Laser Analysis and Design (GLAD) by Applied Optics Research (http://www.aor.com). GLAD represents the optical beam by the complex amplitude of the optical wavefront and calculates the performance of systems with a well-defined direction of propagation.[9] It is a three-dimensional code that represents the two transverse directions as two-dimensional arrays and the axial direction by successive calculations (*i.e.*, it is a sequential ray-trace program). The present analysis does not include telescope pointing or atmospheric seeing, although both effects could be added at a later time.

The optical system shown in Figure 1 was entered into GLAD by placing each element in three-space using its absolute coordinates. The folded, reflective system was modeled, rather than the lens-equivalent model shown in Figure 2, in order to retain aberrations, facilitate baffle placement, and speed computations (*i.e.*, each powered reflective surface would need to be replaced by two refractive surfaces). The SOFIA telescope was modeled as an obscuring head ring, an obscured primary, an obscured secondary, and a reflective tertiary with the secondary as the system stop and its central 'button' as the largest obstruction. The spectrometer elements from DW to DD were included; each element was fitted with a clear aperture that could be inserted or removed, as desired. The principal output from GLAD is a ray trace of the central (or gut) ray hit on each surface and two-dimensional plots of the corresponding beam intensity distributions. The plots are displayed in beam-centered coordinates, so a circular beam striking an inclined flat appears circular and, if the beam strikes an optic off center, the optic is offset in the plot (*cf* Figure 6).

On-Axis Performance with a Narrow Entrance Slit: GLAD was used to evaluate the optical throughput assuming the baseline apertures and slits, and to explore options for improvement. Table 1 shows the aperture configurations for seven illustrative cases, all of which trace the central (on-axis) field at a wavelength of 210 μm. Figure 4 displays the beam intensity distributions at five key surfaces for each of the seven cases. The intensities in this figure are logarithmic and are normalized to unity at the peak (black); the grey scale shows three decades. Each intensity distribution in columns 1, 3, and 5 of Figure 4 displays a 1 × 1-inch region centered on the beam. The distributions in columns 2 and 4 have the alternate sizes (in inches) indicated in their upper right-hand corners.

Table 1. Aperture and Slit Size and Placement

Case	Clear Apertures (blank = none, X=baseline, E = enlarged)			Slit Widths (in mm)		Comments
	Front-End	Predisperser	Echelle	PS	ES	
A						No apertures or slits
B	X	X	X	3.7	4.0	Baseline apertures & slits
C	X			3.7		Effects of PS slit
D	X	X		3.7		Effects of predisperser apertures
E	X	X	X	3.7	6.1	Baseline + wider ES slit
F	X	E*		3.7		Effects of enlarged P2 & PP apertures
G	X	E*	X	3.7	6.1	Baseline + enlarged P2, PP, & ES

* The predisperser collimating mirror P2 is enlarged by 7.6 mm in the dispersion direction for the incoming beam and the semimajor axis of the elliptical baffle at PP, the predisperser pupil stop, is enlarged by 12.7 mm.

Case A, which has no apertures or slits within the instrument, features well-formed images of the telescope secondary at the pupils PG and EG and telescope diffraction patterns at the field stops PS, ES, and DD – there is no clipping within the instrument and consequently no additional diffraction – the ideal case!

Case B has baseline apertures throughout the instrument, the PS slit sized to pass half the light from the telescope (~0.7 λ/D), and the ES slit minimally sized per the geometric discussion in §3. All reflections and transmissions are assumed to be 100% efficient and the integrated beam intensity is normalized to unity just before entering the dewar window (DW). Figure 5 shows the throughput in the rear of the instrument after each surface encounter. Ignoring a 4% light loss in the front end, the primary losses occur at surfaces PS, PP, ES, and E4 (the pupils are actually at PG and EG, but the bulk of the clipping occurs at the prior surfaces, PP and E4, respectively). Only 17% of the input light reaches the focal plane at DD. Once diffraction occurs at PS, clipping at each subsequent pupil/field stop leads to additional diffraction at the downstream field/pupil stops, magnifying the initial loss.

To illustrate, Case C has all apertures removed beyond PS and Case D has all apertures removed beyond P2_2. For Case C, the beam patterns at ES and DD are images of the PS slit, including aberrations intrinsic to the design – there are no slits at these locations. The beam patterns at PP and E4 exhibit gross transverse enlargements as a result of the severe clipping at PS (note the scale changes in Figure 4 for PP and E4 relative to the other cases). Elimination of the light loss at these pupils would require a fourfold enlargement of the optics, which is impractical, particularly for the large echelle.

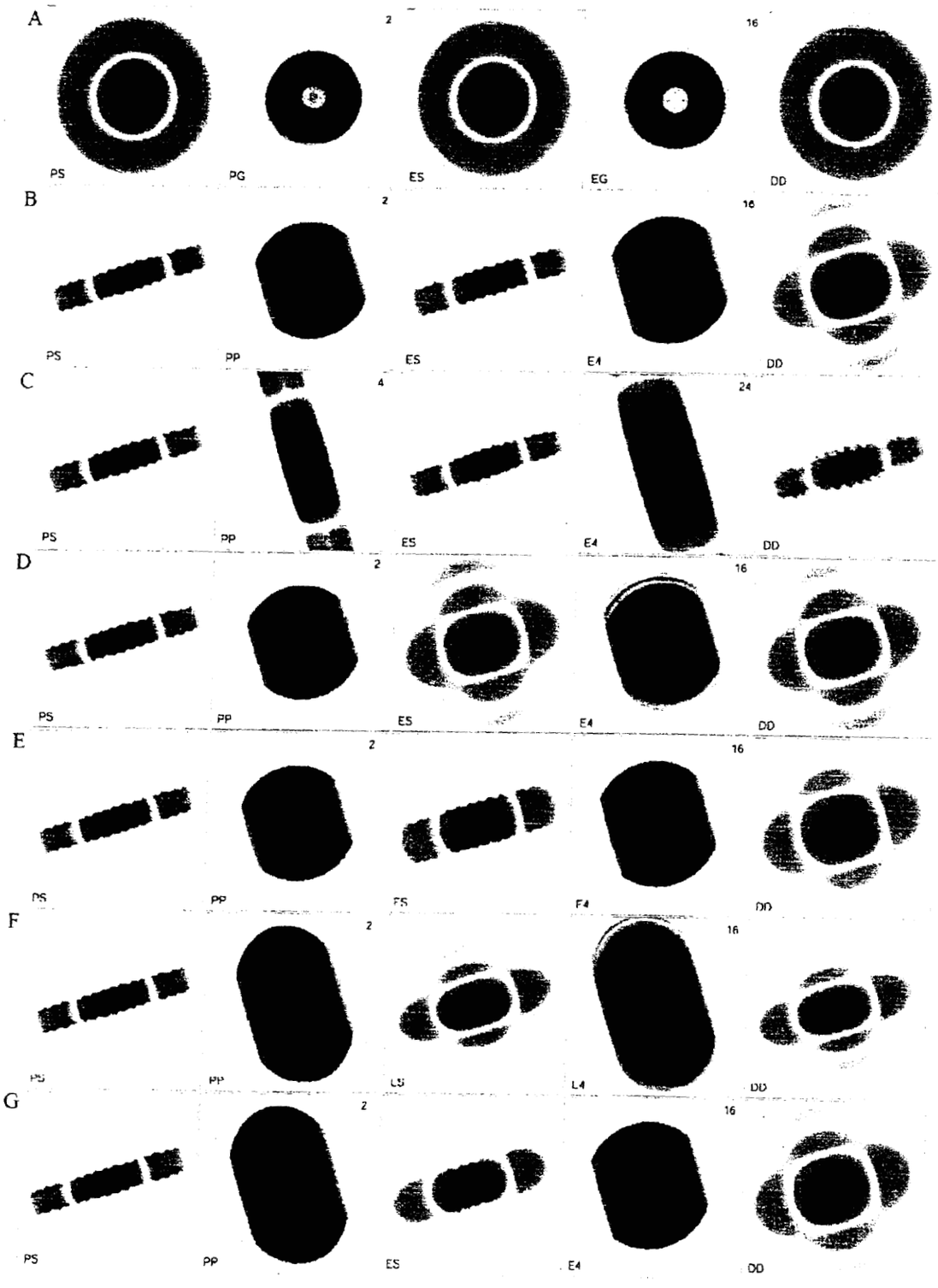

Figure 4. The two-dimensional logarithmic intensity distribution is shown at five key surfaces in the spectrometer for the seven different cases defined in Table 1 and discussed in the text.

Case D shows that clipping the bloomed pupil image in the predisperser, primarily at surfaces P2 and PP, results in additional blooming at ES (compare the intensity distributions for Cases C and D). Similarly, clipping at the field stop ES induces additional blooming at the next downstream pupil (EG).

Case F shows that a modest oversizing of the predisperser optics (see Table 1 footnote) significantly reduces the spot size at the ES slit (compare the intensity distributions for Cases D and F). Not only does this allow more light to pass through an ES slit of fixed width, but the reduced clipping at ES means less blooming in the echelle system as well. Nevertheless, significant clipping must still occur, as the image of PG at EG is much larger than can be passed (compare the large unclipped image at E4 for Case F with the size of the E4 aperture indicated by the clipped image in Case B).

Finally, Cases E and G complete the Case D and F instrument configurations, respectively, by adding apertures to all remaining surfaces. The echelle assembly employs baseline apertures, but the ES slit is oversized relative to Case B (see Table 1). Figure 5 shows that enlarging the predisperser optics is worthwhile, even though the predisperser pupil is then oversized relative to E4 and EG, because Case E passes 27% of the input light, while Case G passes 34% with virtually no change in resolution. Hence, with rather modest design changes, the throughput for the backend of the spectrometer has been increased by a factor of two when used with the narrowest available entrance slit.

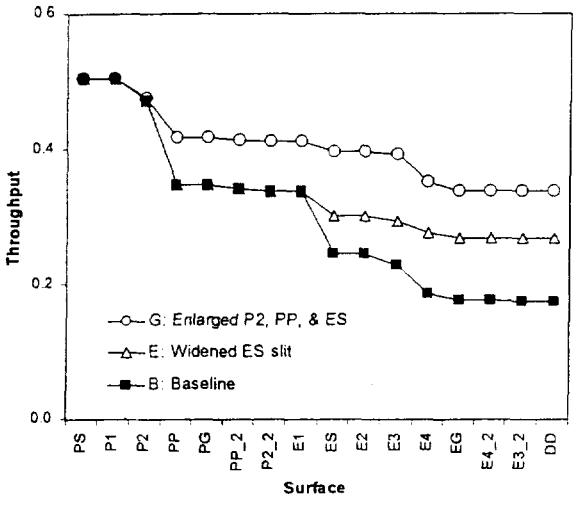

Figure 5. The throughput after each surface is shown for the three fully apertured cases in Table 1, starting at the predisperser entrance slit (PS), where half the light is lost, and ending in the spectroscopic focal plane (DD).

Off-Axis Performance: The instrument configuration corresponding to Case G was used to evaluate the off-axis performance of the spectrometer. This represents a 'worst case scenario' in the sense that it assumes a very narrow PS slit width at the longest operating wavelength (210 μm). The off-axis field angle was 84 arcsec; this field strikes the 60-mm long PS slit 25.4 mm off-center and illuminates the outer edge of the detector's field of view at DD. Figure 6 shows the resulting beam intensity distributions at 20 surfaces throughout the spectrometer. The beam is clipped at the first surface (DW) and again at the second surface (TS), passing light only slightly beyond the second Airy null and reducing the throughput to 94%. The intensity distributions at F1, C1, and K1 are clearly distorted, but the pupil at K2 is well formed and easily accommodated by the 10% oversizing at this stop. This distortion is also apparent at surfaces K3, F2, and C2 and additional clipping occurs at C2, but the clipping at the PS slit is so severe that this relatively gentle 'preclipping' simply doesn't matter. After PS, the off-axis throughput is 96% of the on-axis throughput (*i.e.*, Case G); this throughput ratio remains constant all the way to the focal plane at DD. As evidenced by the asymmetry in the beam pattern at DD, these differences in throughput can be almost entirely eliminated by lengthening the PS and ES slits, but not by increasing DW, TS, or any of the other front-end apertures.

Nevertheless, it is prudent to increase these first two apertures somewhat, even though similar clipping then occurs at other surfaces ahead of PS, because surface DW is attached to the dewar and surface TS is attached to the cryogenic baseplate. Any relative motion of these two softly connected surfaces is likely to produce radiative microphonics and lead to excess noise. Fortunately, this change is easily accommodated by the mechanical design.

The difference between the on- and off-axis throughput decreases with wavelength, since the slit lengths and front-end apertures become effectively more oversized in terms of Airy rings. This is well matched to present detector capabilities. At long wavelengths current arrays have pixel-to-pixel responsivity variations of 50% or greater so small variations in illumination are relatively unimportant. At shorter wavelengths, readily available commercial arrays are extremely uniform and such throughput variations would be more troublesome.

Some other interesting diffraction-related details are evident in Figure 6 that were not readily apparent from the limited number of surfaces shown in Figure 4. For example, EG is undersized relative to E4, so clipping occurs at both surfaces. The 7.6-mm oversizing at the top of P2 (see footnote to Table 1) has clearly been advantageous, but a similar extension is not required at the bottom of P2_2 (*i.e.*, same physical mirror, second pass) because clipping at PP has decreased the beam size. Mirror E3 is sufficiently oversized to avoid any significant clipping; the beam is much smaller on the return pass (*i.e.*, surface E3_2) after clipping at E4/EG.

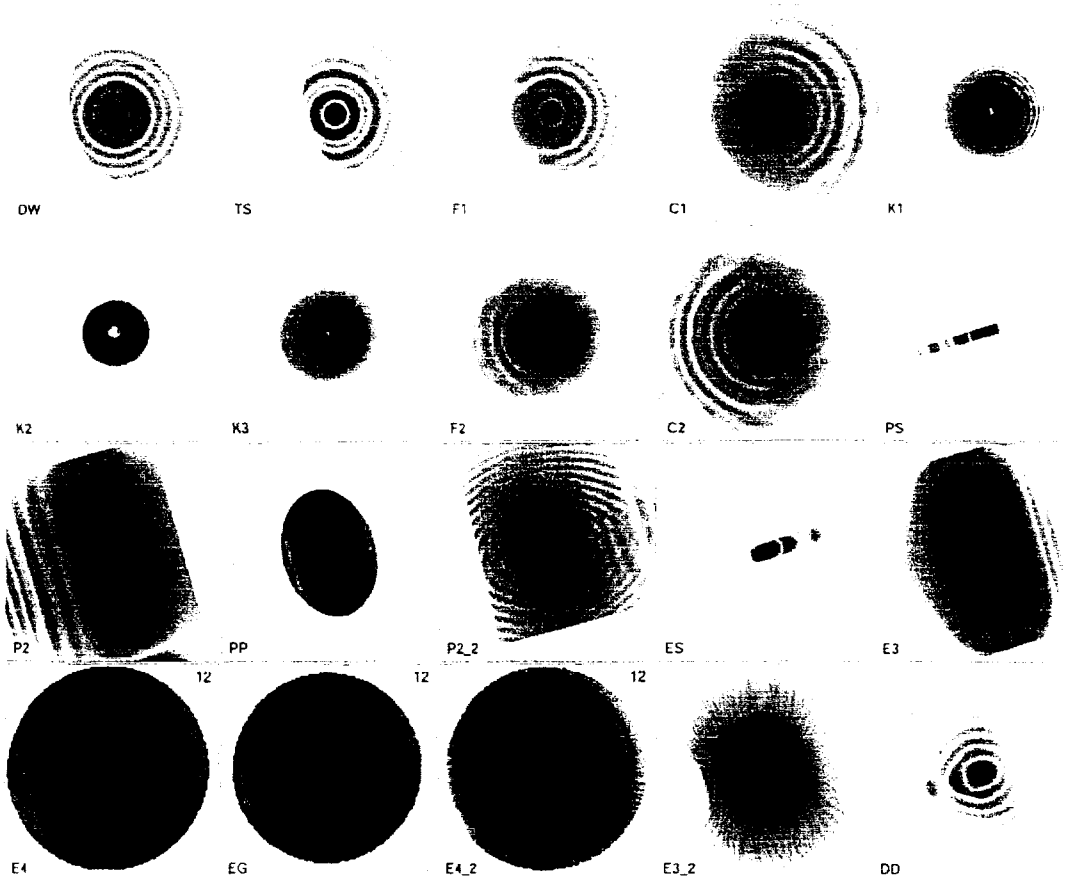

Figure 6. The two-dimensional logarithmic intensity distributions are shown at 20 surfaces in the spectrometer for off-axis illumination. The intensities are normalized to unity at the peak (black) and the grey scale shows four decades. Each panel displays a 3 × 3-inch region centered on the beam, except where a different size (in inches) is indicated in the upper right-hand corner.

Perfomance with Wider Slits: For a fixed grating length, the best strategy for improving throughput is to simply open up the slits. The previous cases (see Table 1) sized the PS slit width so that half the light was lost in an effort to deliver the maximum possible resolution and to ascertain the throughput under a 'worst case scenario'. As the PS slit width is increased, the blooming and subsequent clipping is significantly decreased at the downstream pupil (PG, EG) and field (ES, DD) stops.

Figure 7 shows the throughputs for a number of PS/ES slit combinations. The PS slit widths considered are Δy_i = 3.7, 4.5, 5.1, 5.9, 6.7, 7.6, and 8.9 mm and the corresponding geometrically-sized ES slit widths are $\Delta y'_j$ = 4.0, 4.7, 5.3, 6.1, 6.9, 7.8, and 9.0 mm. For PS slit width i, ES slits widths i, ..., 8 are allowed by Equation (5). The filled circles show the system throughput calculated by GLAD for the front end of the instrument, up to and including the clipping at the PS slit. The solid curve was obtained by integrating the point spread function in Equation (1), assuming an infinitely long PS slit. The GLAD results are in excellent agreement with this 'prediction'. The small, horizontal dashes are the GLAD

throughputs at the detector focal plane (DD) for the minimum-sized ES slit and for all larger slits, including an infinite width slit (*i.e.*, for each PS slit width Δy_i, the associated ES slit widths are $\Delta y'_j$, $j \geq i$ and ∞ (*i.e.*, no slit)). An upper limit to the throughput at DD is quickly reached, so the values for the larger ES slit widths fall on top of each other. The envelope defined by the dashes gives the range of expected throughputs for the instrument as a function of PS slit width. For example, for a PS slit width of 3.7 mm, the total system throughput can be increased from 25% to 37% by increasing the ES slit width. Similarly, the total system throughput can be increased from 37% to 75% by increasing the PS slit width from 3.7 mm to 8.9 mm.

The penalty for opening up the ES slit is increased scattered light emanating from the predisperser, both in the selected echelle order and in adjacent orders. The leakage in adjacent orders could be estimated with GLAD, but is not expected to be significant.

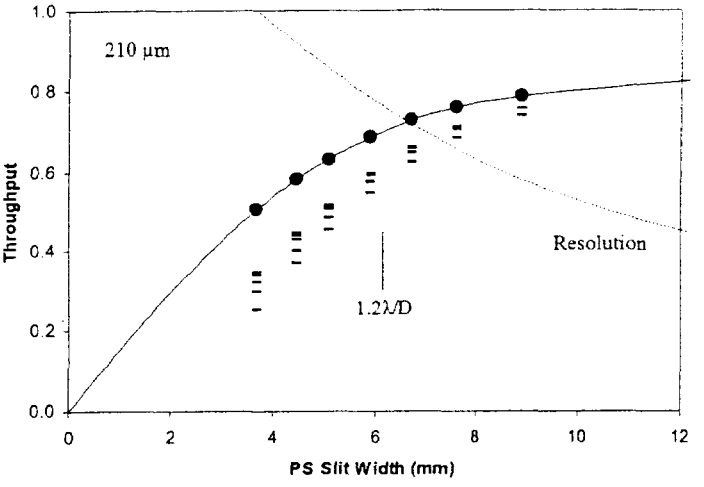

Figure 7. The instrument throughput is shown as a function of PS slit width. Filled circles are throughput after PS and dashes are throughput at the detector assuming various ES slit widths (see text). The dashed line shows normalized resolution, also as a function of PS slit width.

The penalty for opening up the PS slit is decreased spectral and spatial resolution. The GLAD-predicted spot size at DD is nearly independent of slit width, implying that the resolution achievable for a point source is constant, assuming there are no guiding errors. However, for a filled entrance slit, the spectral resolution was estimated by combining these spot widths with the corresponding slit widths in quadrature. The inferred resolution, shown by the dotted line in Figure 7, was normalized to unity for a PS slit width of 3.7 mm. The trade-off is now clear – a factor of two in throughput can be exchanged for a factor of two in resolution. Different investigations may choose different slit widths in order to best meet their scientific objectives.

5. CONCLUSIONS

The light loss in a grating spectrometer with an entrance slit width of ~λ/D is dominated by internal diffraction, rather than telescope diffraction, unless its optics are grossly oversized. Since AIRES is designed to change slit widths and remain near this diffraction limit over its entire wavelength range, the internal light loss at 17 μm can be just as large as at 210 μm.

If aggressively narrow slits are employed, the additional light lost within the instrument can exceed that initially lost at the entrance slit, since diffraction at one surface leads to clipping, and therefore additional diffraction, at downstream surfaces. Under these circumstances, modest enlargements of the predisperser optics and exit slit can increase the instruments' throughput by a factor of two relative to that for the baseline apertures with no sacrifice in resolution.

For a fixed spectrometer volume and grating size, the best compromise between resolution and throughput requires significant internal light loss, very unlike the situation for imagers, where light loss is usually minimal.[4,5] The resolution-throughput product for AIRES is maximized near 1.2 λ/D for the minimum-sized geometric slit widths in §3, but is maximized near λ/D when the ES slit widths are appropriately widened by ~50%.

A physical optics program such as GLAD is an essential tool for understanding these diffraction effects and minimizing their impact on performance in a complex instrument such as AIRES.

ACKNOWLEDGEMENTS

The author gratefully acknowledges S. Colgan and E. Erickson for useful discussions and their comments on the manuscript; D. Lynch, J. McGuire and D. Hasenauer for their early work on the optical design; D. Hasenauer, J. Isenberg, and the rest of the ORA technical support group for their invaluable assistance in using Code V; and G. Lawrence for his help with the initial transfer of the optical design from Code V to GLAD and for his continuing technical support.

APPENDIX A: THE AIRES' GRATING CONFIGURATIONS

The general grating equation is $m\lambda = d\ (\sin\alpha + \sin\beta)\cos\gamma$, where α and β are the input and output angles projected onto the dispersion plane and γ is the out-of-plane angle.[10] The AIRES' echelle is operated in quasi-Littrow mode, so the central field has $\alpha = \beta$ and $\gamma \approx 0.5°$ and the above equation reduces to $m\lambda = 2d' \sin\beta$, where $d' = d\cos\gamma \approx d$. The AIRES' predisperser is operated in non-Littrow mode, so the central field has $\gamma = 0$, $\alpha = \eta - \zeta$, and $\beta = \eta + \zeta$, where η is varied to change wavelengths and $2\zeta \approx 4°$ is the fixed angular difference between α and β. Substitution and simplification gives $m\lambda = 2d'' \sin\eta$, where $d'' = d\cos\zeta \approx d$. Hence, the grating equation for the central field has the same form in both cases, provided the mean angle $\eta = (\alpha + \beta)/2$ is used.

Variations in γ along the slit can cause both field rotation and field curvature.[7] Field rotation is eliminated in the predisperser by making $\gamma = 0$ at the centers of the PS and ES slits, but field curvature remains and varies with η (see §3). Both modest field curvature and rotation occur in the spectroscopic focal plane (DD) as EG is articulated.

The resolution of a grating spectrometer is derived by differentiating the grating equation with respect to β and dividing the result into the original to obtain $R = \lambda/\delta\lambda = (\sin\alpha + \sin\beta)/(\cos\beta\,\delta\beta)$. For the central echelle field this reduces to $R = 2\tan\beta/\delta\beta$ and for the central predisperser field substitution yields $R = 2\tan\eta/(\delta\eta\,(1+\tan\eta\tan\zeta)) \approx 2\tan\eta/\delta\eta$. Hence, in either case, $R = \lambda/\delta\lambda \approx 2F\tan\eta/\delta y$, using the mean angle $\eta = (\alpha + \beta)/2$ and $\delta y = F\,\delta\eta$, the definition of focal length (F). The quantity $\delta\eta$ has major contributions from the entrance slit width (PS) and from diffraction in the echelle system. For an infinitely narrow slit, $\delta\eta = 1.02\,\lambda/D'$, where D' is the diameter of the beam on the collimator E4.[11]

REFERENCES

1. M. R. Haas, E. F. Erickson, J. A. Baltz, S. W. J. Colgan, D. H. Lynch, J. McGuire, R. K. Piña, T. L. Roellig, J. P. Simpson, C. M. Telesco, J. Wolf, and E. T. Young, "The preliminary optical design for AIRES: an Airborne InfraRed Echelle Spectrometer for SOFIA," *SPIE*, **3354**, pp. 940-951, 1998.
2. E. F. Erickson, S. Matthews, G. C. Augason, J. R. Houck, M. O. Harwit, D. M. Rank, & M. R. Haas, "All-aluminum optical system for a large cryogenically cooled far infrared echelle spectrometer," *SPIE*, **509**, pp. 129-139, 1984.
3. K. G. Bach, B. W. Bach, and B. W. Bach, Jr., 'Large Ruled Monolithic Echelle Gratings', *SPIE*, **4014**, pp. 118-121, 2000.
4. L. Keller, "Optical design details and analysis," FORCAST Technical Memo TM-FOR00-29 (http://tnt.tn.cornell.edu /techmemos/TM-FOR00-29.doc), 2000.
5. D. A. Harper *et al.*, "HAWC – a far-infrared camera for SOFIA," *SPIE*, **4014**, pp. 43-53, 2000.
6. M. Born and E. Wolf, *Principles of Optics*, Pergamon Press, Oxford, 1964.
7. J. F. James and R. S. Sternberg, *The Design of Optical Spectrometers*, Chapman & Hall, London, 1969.
8. E. Hecht, *Optics, Third Edition*, Addison Wesley Longman, Inc., Massachusetts, 1998.
9. G. Lawrence, *GLAD Theory Manual*, Version 4.7, Applied Optics Research, Washington, 2002.
10. D. J. Schroeder and R. L. Hilliard, "Echelle efficiencies: theory and experiment," *Applied Optics*, **19**, pp. 2833-2841, 1980.
11. E. F. Erickson and D. Rabanus, "Beam shape effects on grating spectrometer resolution," *Applied Optics*, **39**, pp. 4486-4489, 2000.